

## A model for the radiative forcing during ACE-Asia derived from CIRPAS Twin Otter and R/V *Ronald H. Brown* data and comparison with observations

William C. Conant,<sup>1</sup> John H. Seinfeld,<sup>1</sup> Jian Wang,<sup>1</sup> Gregory R. Carmichael,<sup>2</sup> Youhua Tang,<sup>2</sup> Itsushi Uno,<sup>3</sup> Piotr J. Flatau,<sup>4,5</sup> Krzysztof M. Markowicz,<sup>6</sup> and Patricia K. Quinn<sup>7</sup>

Received 30 November 2002; revised 24 February 2003; accepted 24 March 2003; published 20 August 2003.

[1] Vertical profiles of aerosol size, composition, and hygroscopic behavior from Center for Interdisciplinary Remotely Piloted Aircraft Studies (CIRPAS) Twin Otter and National Oceanic and Atmospheric Administration R/V *Ronald H. Brown* observations are used to construct a generic optical model of the Asian Pacific Regional Aerosol Characterization Experiment (ACE-Asia) aerosol. The model accounts for sulfate, black carbon, organic carbon, sea salt, and mineral dust. The effects of relative humidity and mixing assumptions (internal versus external, coating of dust by pollutants) are explicitly accounted for. The aerosol model is integrated with a Monte Carlo radiative transfer model to compute direct radiative forcing in the solar spectrum. The predicted regional average surface aerosol forcing efficiency (change in clear-sky radiative flux per unit aerosol optical depth at 500 nm) during the ACE-Asia intensive period is  $-65 \text{ W m}^{-2}$  for pure dust and  $-60 \text{ W m}^{-2}$  for pure pollution aerosol (clear skies). A three-dimensional atmospheric chemical transport model (Chemical Weather Forecast System (CFORS)) is used with the radiative transfer model to derive regional radiative forcing during ACE-Asia in clear and cloudy skies. Net regional solar direct radiative forcing during the 5–15 April 2001 dust storm period is  $-3 \text{ W m}^{-2}$  at the top of the atmosphere and  $-17 \text{ W m}^{-2}$  at the surface for the region from  $20^\circ\text{N}$  to  $50^\circ\text{N}$  and  $100^\circ\text{E}$  to  $150^\circ\text{E}$  when the effects of clouds on the direct forcing are included. The model fluxes and forcing efficiencies are found to be in good agreement with surface radiometric observations made aboard the *R.H. Brown*. Mean cloud conditions are found to moderate the top of atmosphere (TOA) radiative forcing by a factor of  $\sim 3$  compared to clear-sky calculations, but atmospheric absorption by aerosol is not strongly affected by clouds in this study. The regional aerosol effect at the TOA (“climate forcing”) of  $-3 \text{ W m}^{-2}$  is comparable in magnitude, but of opposite sign, to present-day anthropogenic greenhouse gas forcing. The forcing observed during ACE-Asia is similar in character to that seen during other major field experiments downwind of industrial and biomass black carbon sources (e.g., the Indian Ocean Experiment (INDOEX)), insofar as the primary effect of aerosol is to redistribute solar heating from the surface to the atmosphere. *INDEX TERMS*: 0305

Atmospheric Composition and Structure: Aerosols and particles (0345, 4801); 1620 Global Change: Climate dynamics (3309); 3359 Meteorology and Atmospheric Dynamics: Radiative processes; *KEYWORDS*: dust, black carbon, direct aerosol forcing, internal mixing, ACE-Asia, radiative transfer model

**Citation:** Conant, W. C., J. H. Seinfeld, J. Wang, G. R. Carmichael, Y. Tang, I. Uno, P. J. Flatau, K. M. Markowicz, and P. K. Quinn, A model for the radiative forcing during ACE-Asia derived from CIRPAS Twin Otter and R/V *Ronald H. Brown* data and comparison with observations, *J. Geophys. Res.*, 108(D23), 8661, doi:10.1029/2002JD003260, 2003.

<sup>1</sup>Department of Environmental Sciences and Engineering, California Institute of Technology, Pasadena, California, USA.

<sup>2</sup>Center of Global and Regional Environmental Research, University of Iowa, Iowa City, Iowa, USA.

<sup>3</sup>Research Institute for Applied Mechanics, Kyushu University, Fukuoka, Japan.

<sup>4</sup>UCAR Senior Visiting Scientist at Naval Research Laboratory, Monterey, California, USA.

<sup>5</sup>Scripps Institution of Oceanography, University of California, San Diego, California, USA.

<sup>6</sup>Institute of Geophysics, University of Warsaw, Warsaw, Poland.

<sup>7</sup>Pacific Marine Environmental Laboratory, NOAA, Seattle, Washington, USA.

## 1. Introduction

[2] Aerosols in the atmosphere, about half of which are of anthropogenic origin, influence the Earth's climate by scattering and absorbing sunlight, and by scattering, absorbing and emitting terrestrial radiation. They have a "direct radiative forcing" which is quantified as the instantaneous perturbation they impose on the net vertical transfer of radiative energy (radiative flux,  $\text{W m}^{-2}$ ), which consists of both solar ( $0.2 \mu\text{m}$  to  $4.0 \mu\text{m}$ ) and terrestrial ( $4.0 \mu\text{m}$  to  $100 \mu\text{m}$ ) radiation. Measured at the top of the atmosphere (TOA), this is called TOA aerosol forcing; measured at the surface, it is called surface aerosol forcing. Globally averaged, aerosol forcing by anthropogenic species is estimated to be about  $-0.3$  to  $-1.0 \text{ W m}^{-2}$  at the top of the atmosphere. Regionally forcing can be stronger than tens of  $\text{W m}^{-2}$ . If the aerosol does not absorb, the surface forcing is approximately equal to that at the TOA. However, certain mineral dusts and black carbon (soot) absorb solar radiation, so that typically, the surface forcing is a factor of 2–3 greater than the magnitude of the TOA forcing [Ramanathan *et al.*, 2001].

[3] Aerosol radiative forcing is very sensitive to aerosol properties, (i.e., mass concentration, size distribution, and absorptive characteristics), as well as environmental conditions, (i.e., surface reflectivity, solar zenith angle, and cloud distribution). Aerosol properties vary widely among various aerosol types (e.g., dust, biomass smoke, urban pollution, sea salt) and geographical regions. To help reduce the presently large uncertainties in estimates of direct aerosol radiative forcing, numerous large field campaigns have been conducted, the most recent of which has been the Asian Pacific Regional Aerosol Characterization Experiment (ACE-Asia) conducted from March to April 2001 in the West Pacific East of China.

[4] East Asia is one of the strongest aerosol source regions, with significant emissions from dust storms, industrial sources, and biomass burning. Likewise, projections of rapid industrialization and population growth throughout Asia suggest this region will be the largest global source of anthropogenic aerosol by 2030 [Houghton *et al.*, 2001]. Among the primary goals of the ACE Asia experiment was to use chemical transport and radiative transfer models to calculate aerosol radiative forcing by this complex and diverse system of aerosols. Ideally, aerosol radiative effects can be determined by directly relating observations of aerosol properties to the effects they have on the radiation field. However, because aerosol properties are highly variable in space and time, because observational sampling is limited in space and time, and because it is difficult to assess aerosol radiative effects in the presence of clouds, estimates of regional radiative forcing must come from a hybrid approach in which models are used to determine the forcing, and observations are used where available to constrain or validate these model predictions. The more physically based these validated models are, the greater confidence we will have in using their predictions under varying emissions scenarios, for which observational constraints are not available.

[5] Direct aerosol radiative forcing ( $A$ ) is defined here as the difference in the net (down minus up) radiative flux between two cases: the first with aerosol present ( $F$ ) and the second "Rayleigh case" where aerosol is not present ( $F_R$ ) [Conant, 2000a],  $A = F - F_R$ . The effects of both natural

and anthropogenic aerosols are included in this definition. The "indirect effects" of aerosol on cloud microphysics are not considered here, although they are expected to be an important contributor to aerosol forcing of climate [Houghton *et al.*, 2001]. Aerosol forcing can be defined at the top of the atmosphere ( $A_T$ ), at the surface ( $A_S$ ), and as the effect on atmospheric heating ( $A_A$ ), which is the difference between TOA and surface forcings when applied to horizontal scales large compared to the tropospheric depth,  $A_A = A_T - A_S$ . Aerosol forcing is often expressed as the product of two observed quantities, aerosol optical depth ( $\tau$ ) and aerosol forcing efficiency ( $\beta$ ) such that  $\beta \equiv A/\tau$ .  $\beta$  can be defined at the surface ( $\beta_S$ ) and at the TOA ( $\beta_T$ ). The ratio  $\beta_S/\beta_T$  is a sensitive indicator of aerosol absorption [Satheesh and Ramanathan, 2000].

[6] Pioneering studies on the direct radiative forcing by Asian aerosols were conducted during the Indian Ocean Experiment, in which observations of aerosol chemistry, optical properties, and sensitivity of radiative fluxes to changes in these properties were combined with sophisticated radiative transfer models to demonstrate: (1) A large plume of biomass and industrial emissions rich in organic and black carbon aerosol is carried by the northeast monsoon over the N. Indian Ocean each winter; (2) this aerosol plume is responsible for a large ( $-15$  to  $-30 \text{ W m}^{-2}$ ) surface radiative forcing over a large fraction of the N. Indian Ocean; and (3) the ratio  $\beta_S/\beta_T$  is large (2–3), indicating that this aerosol plume was far more influential on the surface radiation budget than on the planetary radiation budget [Jayaraman *et al.*, 1998; Podgorny *et al.*, 2000; Conant, 2000a, 2000b; Satheesh and Ramanathan, 2000; Ramanathan *et al.*, 2001; Collins *et al.*, 2002]. Among the goals of the present study will be to compare and contrast the salient processes controlling aerosol radiative forcing between ACE-Asia and INDOEX, each of which represents areas downwind of Asian regions characterized by extensive use of biomass fuels, rapid industrialization, and dense populations.

[7] The data used in this paper comprise aerosol physical chemical, and optical properties and radiometric fluxes observed from two platforms during ACE-Asia (Figures 1a and 1b): (1) the Center for Interdisciplinary Remotely Piloted Aircraft Studies (CIRPAS) Twin Otter aircraft, which flew 19 research flights out of Iwakuni Marine Corps Air Station from 31 March to 1 May 2001 and (2) the National Oceanic and Atmospheric Administration (NOAA) R/V *Ronald H. Brown*, which cruised from Honolulu Hawaii on 14 March 2001 into the Sea of Japan and back through the Straits of Korea terminating at Yokosuka, Japan on 20 April 2001. This combination of surface and airborne platforms provides unique insight into the horizontal and vertical variations in aerosol physicochemical properties. A description of the Twin Otter data is given by Wang *et al.* [2002], and the *R.H. Brown* data used here are introduced by Markowicz *et al.* [2003]. These data are used to construct an aerosol radiative forcing model, which is then used with the Chemical Weather Forecast System (CFORS) [Uno *et al.*, 2003] chemical transport model, which predicts the regional distribution and composition of aerosol.

[8] The strategy taken in this study is outlined here: (1) Construct an optical model consistent with Twin Otter and *R.H. Brown* observations of aerosol size, chemistry, single-scatter albedo, hygroscopicity, and mixing state.

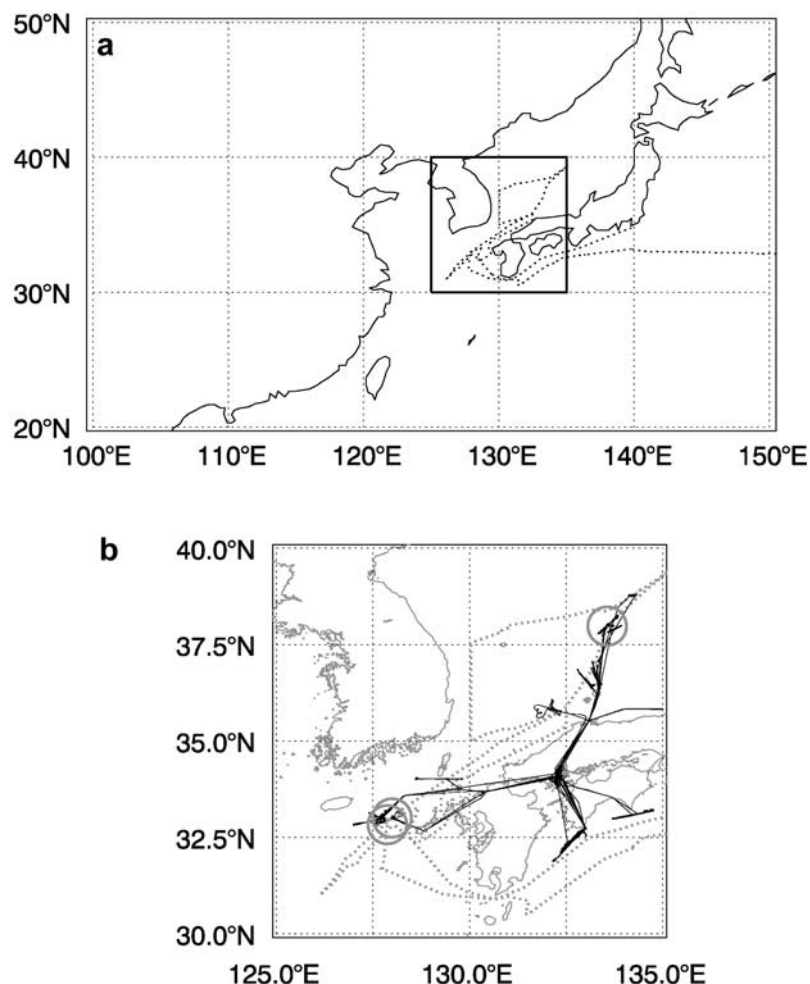


**Figure 1.** (a) Map of the larger ACE-Asia region. Estimates of regional radiative forcing in this paper pertain to this region. The cruise track of the NOAA R/V *R.H. Brown* is shown as a thick dotted line. The box represents the CIRPAS Twin Otter operating area that is expanded in Figure 1b. (b) Map of the intensive research area where the Twin Otter operated. The *R.H. Brown* cruise track is shown as a thick dotted line. The 19 flights of the Twin Otter are overlain as the thin tracks that emanate from Iwakuni MCAS near Hiroshima, Japan. Thick gray circles identify locations where the Twin Otter flew within 10 km of the *R.H. Brown*.

(2) Couple the aerosol optical model to a Monte Carlo Radiative Transfer Model [Podgorny *et al.*, 2000] to predict radiative forcing and forcing efficiency for each of the species and combinations of these species. (3) Determine the sensitivity of aerosol forcing to assumptions about aerosol mixing state, coating of mineral dust by combustion/biomass aerosol, and cloudiness. (4) Couple the radiative forcing predictions to the CFORS chemical transport model to predict the optical properties and radiative forcing by five aerosol types (sulfate, organic carbon, sea salt, mineral dust, and black carbon) during the 5–15 April 2001 dust storm period. (5) Evaluate the forcing predictions against radiometric observations of optical depth and forcing efficiency made from the *R.H. Brown*. (6) Compare and contrast the key features of aerosol forcing in the ACE-Asia region to those in the INDOEX region.

## 2. Aerosol Optical Model

[9] To compute aerosol radiative forcing, the following aerosol properties must be estimated: column burden of

aerosol by type ( $\text{kg m}^{-2}$ ); vertical distribution of this burden ( $\text{m}^{-1}$ ); single-scatter properties of the aerosol, namely mass extinction efficiency  $k_e$  ( $\text{m}^2 \text{kg}^{-1}$ ), single-scatter albedo  $\omega_0$ , and scattering phase function  $P(\theta)$  ( $\text{Sr}^{-1}$ ) (note that aerosol optical depth ( $\tau$ ) is equal to the product of the column aerosol burden with a weighted vertical average of  $k_e$ ); spectral variation of these single-scatter properties through the solar and infrared; and the effect of hygroscopic growth on the single-scatter properties.

[10] The following models are used as the basis for the calculations of these properties. CFORS is a multitracer, on-line, system built within the RAMS mesoscale meteorological model [Pielke *et al.*, 1992]. In CFORS multiple tracers are run on-line in RAMS, so that all the on-line meteorological information such as 3-D winds, boundary-layer turbulence, surface fluxes and precipitation amount are directly used by the tracer model at every time step. As a result, CFORS produces with high-time-resolution 3-D fields of tracer distributions and major meteorological parameters. The CFORS chemical transport model predicts the concentration of sulfate, organic carbon, black carbon,

mineral dust and sea salt. The Optical Properties of Aerosols and Clouds (OPAC) [Hess *et al.*, 1998] database provides the baseline size distributions, indices of refraction, single-scatter properties, and hygroscopic properties for water-soluble aerosols (sulfate and soluble organics); black carbon; mineral dust (in four size modes) and sea salt (in two size modes). We use the ACE-Asia observations to modify this database where appropriate. A coated (two-layer) sphere solution to light scattering [Toon and Ackerman, 1981] coupled with the ISORROPIA aerosol chemical equilibrium model [Nenes *et al.*, 1998] is used to calculate aerosol single-scatter properties and their hygroscopic dependence for cases in which the OPAC properties are not consistent with the ACE-Asia observations. These cases include: less absorptive mineral dust; internal mixing of black carbon with sulfate and organic carbon; revised size distributions for this internally mixed case; and coating of mineral dust by sulfate, organic carbon, and black carbon. ISORROPIA predicts the equilibrium water content of aerosol assuming fixed ambient relative humidity (<99%) and an internally mixed composition limited to the following ions:  $\text{NH}_4^+$ ,  $\text{Na}^+$ ,  $\text{Cl}^-$ ,  $\text{NO}_3^-$ ,  $\text{SO}_4^{2-}$ .

[11] A number of observations are used to evaluate the above models. Size distribution measurements from 15 nm to 15  $\mu\text{m}$  made aboard the Twin Otter aircraft between the surface and 4 km in marine layers, dust layers, and aged pollution layers [Wang *et al.*, 2002] are used to classify typical aerosol size distribution for each of these conditions. Accurate representation of aerosol size is critical for mass scattering efficiency, phase function, and spectral dependence of aerosol properties. *R.H. Brown* measurements of single-scatter albedo measured in dust storm conditions show that dust single-scatter albedo ranged from 0.93 to 0.98 (<10  $\mu\text{m}$ ; ambient relative humidity), much higher than the dust single-scatter albedo predicted by the OPAC model. This higher single-scatter albedo is also consistent with remote sensing retrievals of dust storms far from anthropogenic sources that infer single-scatter albedos in excess of 0.9 [Kaufman *et al.*, 2001]. Thus the imaginary index of refraction of dust aerosol is modified (Figure 2) for consistency with these observations. Twin Otter and *R.H. Brown* measurements of single-scatter albedo in heavily polluted conditions consistently find a value near 0.80 for dry aerosol [Mader *et al.*, 2002] and 0.86–0.92 for aerosol at 55% relative humidity [Markowicz *et al.*, 2003]. The dry single-scatter albedo values reported here for the Twin Otter are at the low end of those reported from other platforms (S. J. Masonis, personal communication, 2002). Black carbon concentration in combustion-derived aerosol will be evaluated against these single-scatter albedo measurements. Tandem DMA measurements on board the Twin Otter expose aerosols of fixed dry size to high relative humidities and observe the increase in aerosol size due to water uptake. Results during flights generally show significant growth of sub-micrometer particles indicative of strong hygroscopicity. Minimal variation in this growth was observed among particles in this size range consistent with uniform particle composition. The data indicate, therefore, that the particles are internal mixtures of the dominant accumulation-mode species (sulfate, organic carbon, and black carbon). Single particle analyses of Asian dust have found the mineral particles are often coated with a layer of

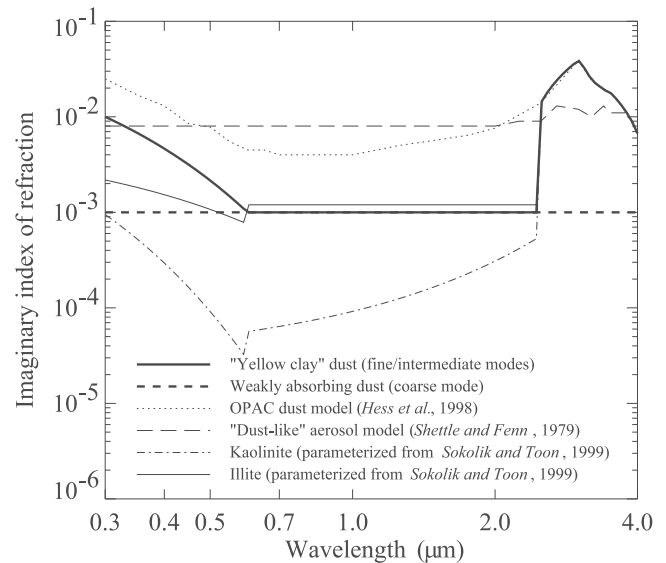


**Figure 2.** Imaginary index of refraction for dust aerosol as a function of wavelength in the solar spectrum. Thick lines (yellow clay and weakly absorbing dust) illustrate the refractive indices used for the ACE-Asia mineral dust model (see text). Thin lines illustrate various published values.

sulfate [Gao and Anderson, 2001]. If this hygroscopic coating leads to addition of aerosol mass by cloud coalescence, then these aerosols will also be coated by carbonaceous species.

[12] The integration of these observations with the optical models is described below. The base for the aerosol optical properties is the Hess *et al.* [1998] OPAC optical package. OPAC provides optical properties for ten monomodal aerosol types. The types used in this study are: water-soluble (comprising tropospheric sulfate and soluble organic carbon), soot, sea salt (two size varieties), and mineral dust (of three size varieties). For each aerosol type, a single lognormal size distribution is specified with a characteristic mode radius and dispersion. Density, index of refraction, and hygroscopic water uptake are specified from literature values. Mie theory is used to calculate single-scatter optical properties from 0.25  $\mu\text{m}$  to 40  $\mu\text{m}$  wavelength and for relative humidities from 0% to 99%. (The assumption that dust particles are spheres does not impart a large bias on the forcing calculations [Mishchenko and Travis, 1994].) These baseline calculations are modified as described below.

[13] Sets of optical properties are determined for three mixing scenarios: (1) external mixing, in which an aerosol population is considered an external mixture of sulfate, organic carbon (OC), black carbon (BC), mineral dust, and sea salt; (2) internal mixing, in which sulfate, OC and BC are combined into a single “combustion aerosol” type (the partitioning among these species is allowed to vary); and (3) coated dust, in which mineral dust is assumed to be coated with a thin layer of combustion aerosol.

## 2.1. External Mixing Case

[14] Aerosol optical properties for the external mixing case are summarized in Table 1. For the external mixing case, sulfate and organic carbon optical properties are taken from

**Table 1.** Single-Scatter Properties for Aerosol Types Used in This Study<sup>a</sup>

Type	$D_m$ , nm	$\sigma$	$k_{es}$ m <sup>2</sup> /g (500 nm; 80% RH)	$\omega_0$ (500 nm; 80% RH)	$k_e$ 80% RH/ $k_e$ dry (500 nm)
water-soluble (used for sulfate and organic carbon)	42	2.24	8.13 (8.10)	.987 (.986)	2.25
soot	24	2.0	10.66 (12.06)	.226 (.350)	1
sea salt (accum.)	418	2.03	4.60 (2.09)	1.000 (1.000)	3.63
sea salt (coarse)	3500	2.03	0.97 (0.42)	1.000 (1.000)	3.87
mineral (fine)	140	1.95	2.79 (1.89)	.986 (.979)	1
mineral (interm.)	780	2.0	0.56 (0.26)	.939 (.893)	1
mineral (coarse)	3800	2.15	0.23 (0.11)	.864 (.791)	1
Externally mixed model (sulfate + OC + BC)			8.28 (8.35)	.928 (.929)	2.15
Internally mixed model (sulfate + OC + BC)	70/150	1.4/1.6	9.52	.905	2.36

<sup>a</sup>The external and internal mixtures correspond only to sulfate, organic carbon (OC) and black carbon (BC) for average concentrations predicted by CFORS over land.  $D_m$  is geometric mean diameter,  $\sigma$  is geometric variance,  $k_e$  is mass extinction efficiency,  $\omega_0$  is single-scatter albedo. The values shown in parentheses are derived from sensitivity study calculations in which  $D_m$  is doubled.

the water-soluble category in OPAC, which consists of a 50/50 mixture of sulfate and soluble organic carbon. Accumulation and coarse modes of sea salt and soot (black carbon) are also taken from the corresponding OPAC categories.

[15] The OPAC size distributions are tested against the Twin Otter Differential Mobility Analyzer (DMA: 0.15–0.5  $\mu\text{m}$ ) and Aerodynamic Particle Sizer (APS: 0.5–15  $\mu\text{m}$ ) composite size distributions presented by Wang *et al.* [2002]. For each of four Twin Otter flights, size distributions are averaged over two or three constant-layer legs. Wang *et al.* [2002] label each leg as one of: free troposphere (dust and pollution), pollution layers, or boundary layer airmasses (which were often polluted). For each leg, a three-mode lognormal size distribution is derived using a nonlinear least squares fitting technique (Table 2). Despite considerable variability, a common feature of each distribution is a mode near 150 nm; most other size distributions also include a smaller mode  $\sim$ 50–70 nm. A wide range of larger modes exist at each layer. The OPAC water-soluble mode (Table 1) best fits the sub-micrometer modes observed by the Twin Otter. The strong 23 nm soot mode in OPAC is not apparent in the observational data, despite evidence of elemental carbon. The absence of this mode is probably due to aging processes, such as aggregation of the soot and internal mixing with the water-soluble particles. Likewise, because OPAC lacks a larger 150 nm “cloud-processed” mode, this will be introduced in the internally mixed case below.

Instead of using the OPAC mineral dust calculations, a new ACE-Asia pure-dust aerosol model is computed from the coated-sphere radiative parameter model to avoid the high levels of dust absorption present in the OPAC model. The only difference between the OPAC and new mineral dust properties is revised imaginary refractive indices across the solar spectrum (Figure 2). We follow OPAC dust size distributions (fine: 0.07  $\mu\text{m}$ , intermediate: 0.39  $\mu\text{m}$ , and coarse: 3.8  $\mu\text{m}$ ) assuming fixed mass ratios (3.4% fine, 76.1% intermediate, 20.5% coarse). (Note that the “fine” and “intermediate” dust modes correspond respectively to the “nucleation” and “accumulation” mineral dust modes in OPAC.) Coarse dust is assumed to be dominated by quartz and calcite based minerals, and thus is specified to be relatively nonabsorptive. The smaller modes (thick solid line) are assumed to have a greater iron oxide and aluminosilicate component (typical of “yellow clay” dusts) and thus have greater absorption in the blue/ultraviolet and near-infrared spectral regions than coarse dust. Note that this ACE-Asia dust representation is considerably less absorptive than conventional dust models [Shettle and Fenn, 1979; Hess *et al.*, 1998], which are illustrated in Figure 2 for comparison. Also shown in Figure 2 are the absorption spectra for common iron-poor minerals (Illite and Kaolinite are shown here; pure Quartz has negligible absorption throughout the solar spectrum; Calcite is transparent to 2.3  $\mu\text{m}$ ). The relatively low imaginary refractive index for

**Table 2.** Parameters (Geometric Diameter, Dispersion, and Concentration) for Three-Mode Lognormal Fits to the Observed Size Distributions From Four Twin Otter Flights<sup>a</sup>

Layer	Flight	Mode 1			Mode 2			Mode 3			RH	$\omega_0$ (Dry)
		$D_m$ , nm	$\sigma$	$N_{As}$ , #/cm <sup>3</sup>	$D_m$ , nm	$\sigma$	$N_{As}$ , #/cm <sup>3</sup>	$D_m$ , nm	$\sigma$	$N_{As}$ , #/cm <sup>3</sup>		
B.L.	11	51	1.25	2277	115	1.75	8022	822	1.84	6	65	
B.L.	12	96	1.53	550	101	1.30	1773	187	1.58	8089	90	
B.L.	14a	69	1.39	7757	142	1.58	4874	283	2.48	75	60	0.73
B.L.	14b	76	1.42	5184	149	1.68	4868	596	2.20	31	50	0.78
P.L.	9	47	1.42	3394	146	1.56	6462	399	2.46	125	70	
P.L.	11	164	1.63	4728	576	1.56	40	1120	1.96	36	50	0.81
P.L.	12	8 <sup>b</sup>	4.20 <sup>b</sup>	14264 <sup>b</sup>	157	1.53	3766	327	1.21	195	20	
F.T.	9	123	1.65	1090	433	2.04	198	4117	1.30	0.5	38	
F.T.	11	140	1.66	1365	571	1.95	131				50	
F.T.	12	74	1.64	686	153	1.57	765	836	1.52	6	10	
F.T.	14	9 <sup>b</sup>	3.86 <sup>b</sup>	2285 <sup>b</sup>	139	1.50	1065				10	

<sup>a</sup>B.L. denotes boundary layer legs, P.L. denotes elevated pollution layers, and F.T. denotes free tropospheric legs normally characterized by mixtures of dust and pollution aerosol. Size distributions were measured at ambient relative humidity (RH). Single-scatter albedo is reported only for durations when elemental carbon was sampled and the particle soot absorption photometer was operational [Mader *et al.*, 2002].

<sup>b</sup>These spurious small diameter modes with large dispersions are artificial, and represent cases where super-micrometer tails in the size distribution are not well represented by a lognormal size mode, but would be better represented by a power law distribution. They are included only to indicate the presence of significant concentrations of super-micrometer aerosols in these layers.

the ACE-Asia dust aerosol is consistent with the relatively low iron fraction in Asian surface soils compared to the global mean [Sokolik and Toon, 1999]. Likewise, observations of dust absorption during ACE-Asia (A. Clarke, personal communication, 2002) and other pollution-free desert regions [Kaufman *et al.*, 2001] are inconsistent with the higher indices of refraction shown in Figure 2 for the Hess *et al.* [1998] and Shettle and Fenn [1979] models. The predicted single-scatter albedo for ACE-Asia dust is 0.94 at 500 nm and 0.98 at 600 nm, which is in far better agreement with the 550 nm measurements of 0.93–0.98 (sub-10  $\mu\text{m}$ , ambient RH) made from the *R.H. Brown* during dust episodes.

[16] It is useful to examine the sensitivity of the optical properties to uncertainties in aerosol size distribution, given that the observations show a high degree of day-to-day variability (Table 2). Claquin *et al.* [1998] show marked sensitivity of radiative forcing to mean radius when number concentration is fixed. However, for the present application, the total aerosol mass and optical depth are estimated with far greater accuracy than the number concentration. Conant [2000b] shows that the forcing is relatively insensitive to uncertainties in aerosol size distribution when optical depth at 500 nm is known. Likewise, we show here that the mass extinction efficiency at 500 nm is also relatively insensitive to uncertainties in size for secondary particles (sulfate, OC, BC). This uncertainty is quantified in Table 1 by re-computing the optical properties of each aerosol type in the external model assuming double the geometric mean diameter ( $D_m$ ). The relatively weak sensitivity of mass extinction efficiency with particle size seen in Table 1 can be understood in the following manner. The mass extinction efficiency is equal to (particle cross-sectional area)  $\times$  (extinction efficiency,  $Q_e$ )/(particle mass). If spectral index of refraction is weakly varying, the Ångström exponent,  $\alpha \equiv -\text{dln}(Q_e)/\text{dln}(\lambda)$ , also yields the diametric dependence  $\alpha \cong \text{dln}(Q_e)/\text{dln}(D_m)$ . Thus we can represent the sensitivity of  $k_e$  to  $D_m$  with,  $\text{dln}(k_e)/\text{dln}(D_m) \cong (\alpha - 1)$ . In polluted ACE-Asia regions,  $\alpha \sim 1$ , and thus there is only a weak dependence of  $k_e$  on uncertainties in diameter. For pure dust, however, size uncertainties are more important, as dust is in a size regime where mass extinction efficiency has an inverse relationship with  $D_m$  ( $\alpha \sim 0$ ).

## 2.2. Internal Mixing Case

[17] For the internally mixed case, optical properties of sulfate, organic carbon, and black carbon are calculated assuming each particle is a homogeneous mixture of the three. On the basis of the size distributions shown in Table 2, the internally mixed “combustion aerosol” is represented with a dry size distribution consisting of two modes: a nucleation mode ( $D_{\text{mod}} = 0.07 \mu\text{m}$ ,  $\sigma = 1.4$ ) and an accumulation mode ( $D_{\text{mod}} = 0.15 \mu\text{m}$ ,  $\sigma = 1.6$ ) with twice as many particles residing in the smaller mode as the larger mode. The relative abundance of sulfate, OC and BC is allowed to vary; for example, the mean mass ratios of sulfate:OC:BC are 18:13:2 over land, and 32:18:3 over ocean. Water uptake by sulfate and ammonium is computed using the thermodynamic equilibrium code ISORROPIA assuming the particles are deliquesced [Nenes *et al.*, 1998]. Spectral indices of refraction are obtained for each component from Hess *et al.* [1998], where the refractive index of sulfate and ammonium is taken from the pure sulfuric acid

component, organic carbon from the “water-soluble” component, and black carbon from the soot component. (Uncertainties related to hygroscopic properties and indices of refraction of organic carbon are large). An effective index of refraction for the soluble components in the mixture (sulfate, soluble organics, ammonium, and water) is computed through volumetric averaging of the molal refraction. An effective index of refraction for the composite pollution aerosol (soluble mixture + black carbon) is computed using the Bruggeman mixing rule.

[18] Figure 3 illustrates the spectral variation of the single-scatter properties of the internally mixed aerosol for comparison with the external mixture for dry aerosol. The increase in optical depth seen in Figure 3a is primarily due to the shifted size distribution relative to the externally mixed case. The most significant feature for the internally mixed case is the known increase in soot absorption efficiency when internally mixed with conservative species [see Chylek *et al.*, 1996; Fuller *et al.*, 1999]. The enhancement in absorption occurs in spite of the introduction of less absorptive sulfate indices of refraction in the internally mixed case, whereas the externally mixed case treats sulfate with the more absorptive water-soluble component from OPAC. Use of the Bruggeman mixing rule may be inappropriate for certain mixtures of black carbon and soluble species [Chylek *et al.*, 1996; Fuller *et al.*, 1999]. When the single-scatter properties are calculated from layered Mie theory, assuming soot is at the core of the mixed particle and sulfate and OC are assumed to form a soluble shell, the absorption is enhanced by 10% beyond the case where the Bruggeman mixing rule is used to determine the single-scatter properties. Thus the use of the Bruggeman mixing rule may be considered a lower limit for absorption in this internal mixing case.

[19] The enhancement in single-scatter albedo decreases with increasing humidity so that the difference at 80% relative humidity is only 0.02 (Table 1). This is not due to a reduction in the enhancement of soot absorption efficiency, but rather occurs because of a compensating increase in the scattering efficiency of the soluble component because the internal mixture is modeled to be slightly more hygroscopic than the external case. (This is not a physical result of the mixing, but is rather an artifact of slight differences between OPAC and ISORROPIA hygroscopic properties). As noted above, these calculations assume 6% black carbon by dry aerosol mass and should not be taken as representative of conditions with different BC fractions.

## 2.3. Coating of Dust

[20] Single particle analysis and transmission electron microscopy (TEM) have shown that sulfates, nitrates, and soluble organic acids often coat the surface of mineral dust particles [e.g., Buseck and Posfai, 1999; Gao and Anderson, 2001; Lee *et al.*, 2002]. It is possible that aging processes, such as cloud processing, which tend to homogenize aerosol properties, will also add soot to the surface of these mineral particles: such mixtures were observed during ACE-Asia (J. Anderson, personal communication, 2002). These effects are modeled in a simple manner by adding a coating of pollution aerosol to dust particles when dust and pollution are mixed and computing single-scatter-properties of this coated dust using layered Mie theory [Toon and Ackerman,

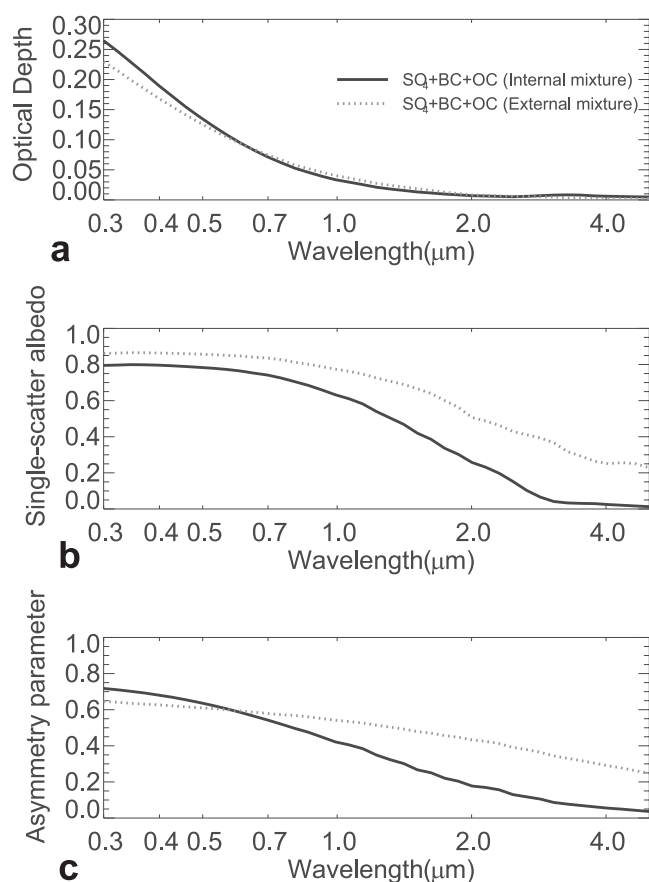


**Figure 3.** Comparison between internal and external mixtures of sulfate, organic carbon and black carbon. Spectral variation for mean conditions are shown for (a) Optical depth, (b) single-scatter albedo, and (c) asymmetry parameter (first moment of phase function). All parameters assume dry aerosol.

1981]. The proportion of combustion aerosol coating the dust is taken from the 2:50 S:Si ratio seen by *Gao and Anderson* [2001] for mixtures of sulfate and Asian dust and the assumed mass fraction of sulfur in the combustion aerosol and silicon in the mineral dust aerosol. This corresponds to 2.7% of the total dust mass. The increase in mass is implemented proportionately across all dust sizes when recomputing optical properties so that the largest dust particles have the largest coating mass. The effect of this coating is to remove some of the aerosol mass (6% for mean conditions over ocean) from the accumulation mode where it is most efficient at scattering radiation. This point is illustrated in Figure 4, which compares the single-scatter properties for the case of coated dust versus the case where equivalent masses of dust and combustion aerosol remain externally mixed. Note that the coating decreases total extinction. Extinction by the coated dust is only 5% greater at 80% relative humidity compared to the dry aerosol.

### 3. Radiative Forcing Model and Predicted Aerosol Forcing Efficiency

[21] The aerosol optical properties described above are integrated within a 38-spectral-band, multiple-scattering

Monte Carlo radiative transfer model, from which aerosol forcing and forcing efficiency are calculated. The model is identical to that described by *Podgorny et al.* [2000] except that the aerosol optical properties have been replaced with those described here. Both Fresnel and bulk scattering by the ocean are implemented such that the ocean albedo matches that of *Briegleb et al.* [1986]. Over land, surface albedo is obtained from April 1987 satellite retrievals by *Sellers et al.* [1996] and is assumed to be Lambertian (Figure 5). Vertical profiles of temperature, humidity, and pressure are obtained from the CFORS calculations except where noted otherwise. Because the interaction between water vapor absorption and aerosol forcing is weak [*Conant, 2000b*], uncertainty in the water vapor absorption has a small effect on the forcing estimates.

[22] As mentioned above, the radiative forcing can be expressed as the product of the aerosol optical depth times an aerosol forcing efficiency,  $\beta$ .  $\beta$  is a relatively stable property sensitive to the single-scatter aerosol properties (primarily single-scatter albedo) and environmental properties (primarily surface albedo and length-of-day) [*Conant, 2000b*]. Unlike radiative flux, which has a linear dependence on the cosine of the solar zenith angle ( $\mu$ ),  $\beta$  is far less sensitive to  $\mu$  because, to a first-order approximation, the reduction in incident flux is compensated for by the increase in optical path through the aerosol layer. However, a

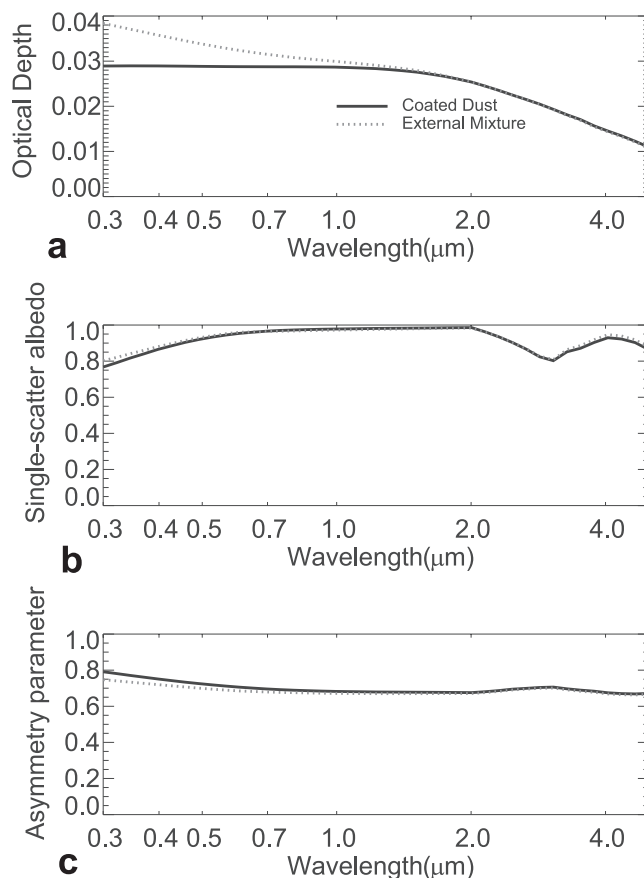


**Figure 4.** Same as Figures 3a–3c, but for the comparison between a mean profile of dust coated with 2.7% (by mass) combustion aerosol against the case where the dust and combustion aerosol remain externally mixed.

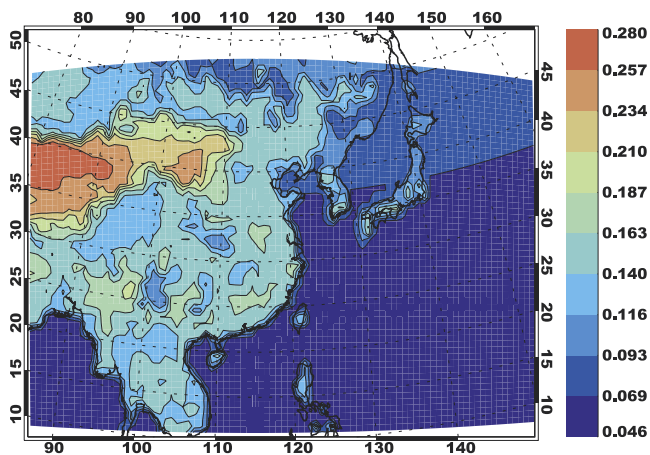


**Figure 5.** April surface albedo. Land albedo is from Sellers *et al.* [1996]. Ocean albedo is predicted by MCRTM as described in text.

second-order sensitivity to solar zenith angle is apparent for thick optical depths and slant zenith angles due to multiple scattering effects and reduction of transmitted radiation. These phenomena combine so that the primary influence of solar ephemeris on aerosol forcing is length of daylight hours, and the influence of solar zenith angle is secondary to day-length. As ACE-Asia was conducted just after the spring equinox, the sensitivity of forcing on latitude due to solar ephemeris is minimal.

[23] Figures 6a–6e illustrate mean results for single-column calculations conducted for the mean meteorological and aerosol profiles in the ACE-Asia region, as predicted by the CFORS model; regional distributions will be illustrated in Section 4. The averages correspond to 5–15 April 2001 over the area 20°N–50°N, 100°E–150°E. During this period, a powerful dust storm carried significant levels of mineral dust mixed with anthropogenic sulfur, OC, and BC over the North Pacific. Figures 6a–6e present the column optical depth, surface and TOA forcing efficiency, and surface and TOA forcing each of the aerosol types during this period.

[24] Averaged over the period 5–15 April 2001, mineral dust is predicted to be the strongest single contributor to the aerosol optical depth and forcing over this region, contributing  $-10 \text{ W m}^{-2}$  to the surface forcing, and  $-6 \text{ W m}^{-2}$  to the TOA forcing. Sulfate and organic carbon (treated together as a “water-soluble” component in the model) have a combined forcing of  $-8 \text{ W m}^{-2}$  at the surface, which is only slightly greater than their  $-7 \text{ W m}^{-2}$  contribution to the TOA forcing. Black carbon is predicted to have a slight ( $0.25 \text{ W m}^{-2}$ ) warming effect at the TOA, yet is a significant source of surface cooling of  $-4 \text{ W m}^{-2}$ . Sea salt forcing contributes only  $-0.5 \text{ W m}^{-2}$  at the surface and TOA.

[25] Mean predicted forcing efficiency by dust is  $-65 \text{ W m}^{-2} \tau^{-1}$ . ( $\tau^{-1}$  denotes per unit optical depth at 500 nm so that units of forcing ( $\text{W m}^{-2}$ ) are not confused with units of forcing efficiency ( $\text{W m}^{-2} \tau^{-1}$ )). This surface forcing efficiency is half that predicted when using the more absorptive OPAC mineral dust model. As a result of the lower absorption, dust contributes significantly to the TOA forcing with a  $\beta_T$  of  $-37 \text{ W m}^{-2} \tau^{-1}$ . Sulfate and OC are

predicted to have comparable surface and TOA forcing efficiencies of  $-30 \text{ W m}^{-2} \tau^{-1}$ , whereas black carbon is far more efficient at reducing surface radiation with a predicted  $\beta_S$  of  $-220 \text{ W m}^{-2} \tau^{-1}$ . Interestingly, the combination of combustion aerosols in this external mixing model (BC + OC + sulfate) has aggregate surface and TOA forcing efficiencies (over ocean) very similar to those of dust at  $-60 \text{ W m}^{-2} \tau^{-1}$  and  $-34 \text{ W m}^{-2} \tau^{-1}$ , respectively. This may explain the relative stability in forcing efficiency values observed from the *R.H. Brown* by Markowicz *et al.* [2003] when the relative contributions of dust and pollution were varying.

[26] The predicted forcing is sensitive to changes between the aerosol model used (external, internal, coated dust) and the presence of clouds (Figure 7). When the internal mixing model is considered, the  $\beta_S$  by combustion aerosol at the surface is increased in magnitude relative to the BC + OC + sulfate contribution predicted by the external model. This is due to the greater atmospheric absorption in the internal mixing scheme. Secondary effects include the change in scattering by including the 150 nm diameter cloud-processed mode to the aerosol distribution and the change in hygroscopic properties between the two models discussed in section 2.2. Considering the third mixing case, in which dust is coated by hygroscopic aerosol (not shown), a small decrease in TOA and surface forcing is seen due to the reduction in sulfate and OC scattering. Atmospheric absorption is relatively unperturbed, as the BC absorption efficiency is not strongly affected by aggregation on the surface of the dust (as predicted by the layered Mie theory).

[27] Clouds have a large effect on the predicted forcing efficiency relative to the clear-sky calculations presented above. Clouds generally decrease the magnitude of TOA forcing relative to clear-sky conditions because of multiple-scattering effects. The effect of clouds on atmospheric absorption however, depends on the vertical distributions of the cloud and aerosol layers. Aerosol absorption is reduced by high clouds, which shade the aerosol, but is enhanced by low clouds, which reflect radiation back up through the absorbing aerosol layers. The effect of clouds on the forcing efficiency in the ACE-Asia region is estimated in the following manner. First, climatological regional albedo is constrained to be 0.325 on the basis of Earth Radiation Budget Experiment [Ramanathan *et al.*, 1989] measurements from April 1985–1989 for the ACE-Asia region (taken here to be 20°N–50°N 100°E–150°E). Three cloud types are considered: low (1 km), middle (4 km), and high (10 km). Relative abundances of these cloud types are determined separately for land (low: 10%, middle: 30%, high: 30%) and for ocean (low: 25%; middle: 20%; high: 30%) on the basis of the 17-year International Satellite Cloud Climatology Project (ISCCP) data set [Rossow and Schiffer, 1991]. As ISCCP does not provide information about subgrid-scale cloud fraction, cloud thickness, or cloud overlap, a range of calculations are conducted spanning a total cloud fraction from 40% to 70% and mean cloud optical depths spanning 10 down to 5. Each calculation is constrained by the ERBE mean regional albedo. These calculations produce a narrow range of forcing efficiency, which is used to estimate forcing efficiency in the presence of these clouds. Correlations between aerosol and cloudiness are assumed to be negligible for this analysis.

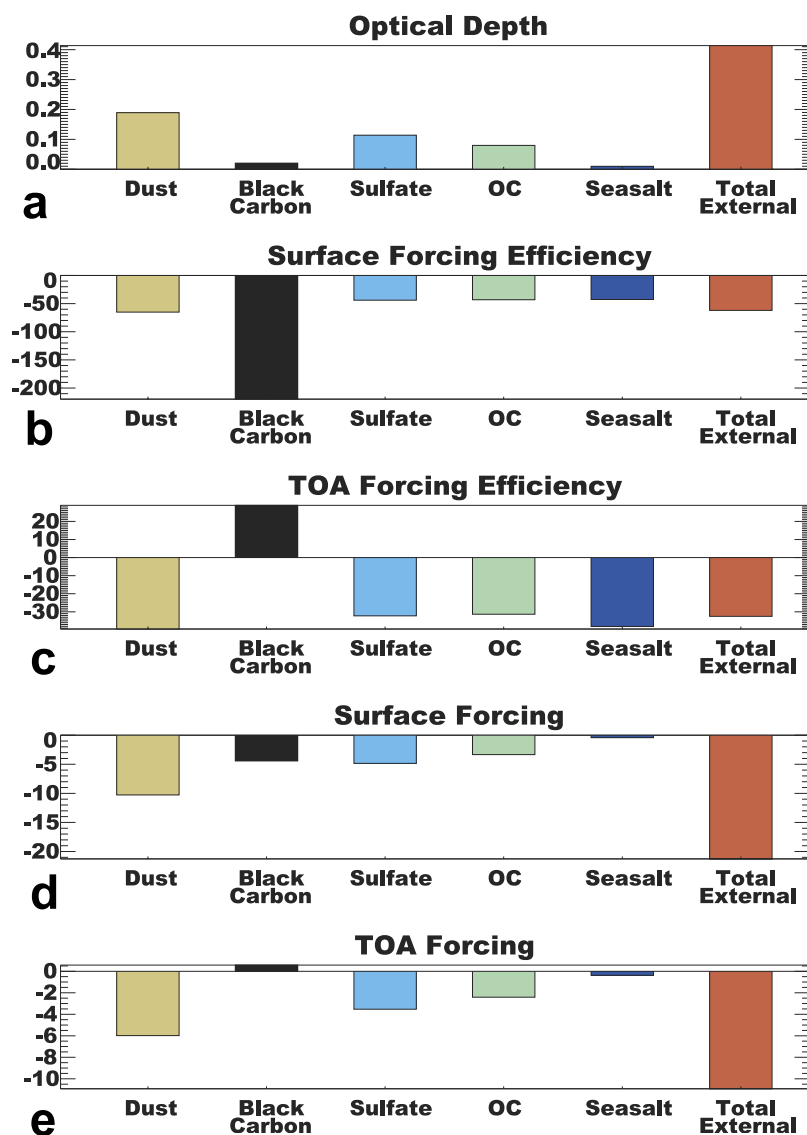


**Figure 6.** Partitioning among species for: (a) optical depth, (b) surface forcing efficiency, (c) TOA forcing efficiency, (d) surface forcing, and (e) TOA forcing. Values are for clear skies using the external mixing model. Data are averaged over the period 5–15 April 2001 for the larger domain shown in Figure 1a.

[28] By reducing the influence of aerosol scattering, cloud increase the predicted surface: TOA forcing ratio from 2.3 in the clear-sky case to 5.7 in the all-sky case. Clouds moderate the TOA forcing by a factor of 3, yet the counteracting effects of low and high clouds result in a negligible effect on aerosol absorption. Surface forcing efficiency is moderated by only 30%.

#### 4. Regional Forcing Estimates

[29] Regional forcing estimates are obtained by applying the radiative transfer model with the ACE-Asia aerosol components to the regional mass distributions of aerosol species predicted by the CFORS model. The ACE-Asia CFORS calculations are described by *Uno et al.* [2003].  $\text{SO}_2$ /Sulfate is predicted using linear chemistry and emissions estimates from *Streets et al.* [2000]. Black carbon and organic carbon are implemented without chemical transformation using emission data from *Streets et al.* [2001]. Sea-

salt is predicted on-line following *Gong et al.* [1997]. Mineral dust is traced in 12 size bins where emission is a function of surface friction velocity and deposition velocity is a function of size.

[30] Aerosol optical depth predicted for the 5–15 April dust storm period is presented in Figure 8a. Also shown are the optical depths partitioned among the individual species assuming external mixing (Figures 8b–8f). (For clarity, the external model is used for the remainder of the calculations except where noted otherwise.) The dominant feature in total optical depth is mineral dust over the Gobi Desert source region where average optical depth over this dust storm period exceeded unity (Figure 8f). Secondary features include the organic sources that reside primarily in southern regions, sulfate sources from fossil fuel burning regions, and black carbon that is associated with both sources. Sea salt optical depth is strongly modulated by ocean surface relative humidity. (The region of low sea salt on the southeastern boundary of the model region is an

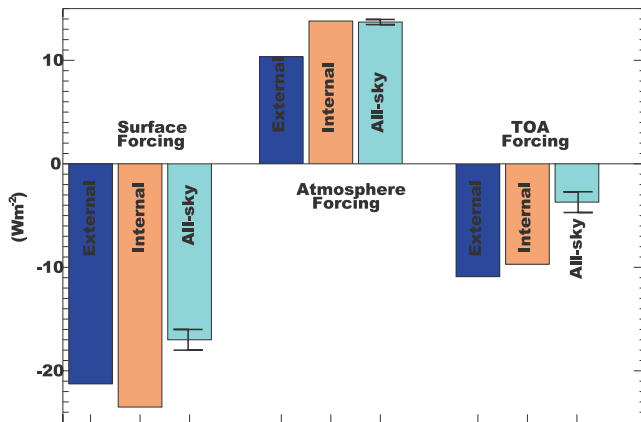


**Figure 7.** Regional forcing at the TOA, the atmosphere and the surface for 3 of the cases described in the text: the externally mixed case (clear-sky), the internally mixed case (clear-sky), and the all-sky (clear and cloudy skies) case. The period and domain are the same as for Figure 6. The range bars for the all-sky cases reflect the sensitivity to cloud fraction described in the text.

artifact, as no sea salt is advected across the boundary into the model domain.)

[31] Mean forcing efficiency ( $\beta$ ) also shows considerable variability over the ACE-Asia domain due to the varying source regions, varying forcing efficiency with aerosol type, and varying effects of humidity, surface albedo, and solar ephemeris on forcing efficiency (Figures 9a–9f and 10a–10f). Surface forcing efficiency ( $\beta_S$ ) for the ACE-Asia aerosol and partitioned among the individual species is shown in Figures 8a–8f. Black carbon radiative forcing is the most efficient at reducing surface radiation, and shows considerable variation due to changes in surface albedo (increased reflection leads to smaller forcing) and solar zenith angle (longer aerosol path leads to a decrease in surface forcing efficiency due to reduction of transmitted radiation). Second most efficient is mineral dust aerosol. Forcing efficiency becomes more moderate with increasing optical depth because of multiple-scattering effects and attenuation of the transmitted radiation. Thus forcing efficiency in the dust source regions is weaker compared to those regions where dust optical depth is  $\ll 1$ . The soluble aerosols: sea salt, organic carbon, and sulfate, each show significant variability in forcing efficiency with relative humidity, consistent with that seen by *Markowicz et al.* [2003]. This effect occurs for two reasons: first, increasing relative humidity increases the water content of the aerosol, moderating the comparatively stronger influence of absorbing aerosol components; second, the increased aerosol size leads to greater forward scattering, which, in turn, leads to smaller forcing efficiency (but not smaller forcing, as will be shown in Figure 11). The moderation in forcing efficiency with increased aerosol loading is also seen in the large OC source regions in and near Southern China. The features of sulfate forcing efficiency are similar to those for organic carbon because the OPAC water-soluble aerosol model is used for both components; however, significant differences are apparent due to the differing sources and transport mechanisms.

[32] Forcing efficiency at the TOA ( $\beta_T$ ) shows a considerably different signature than at the surface because at the

surface aerosol absorption and scattering combine to reduce solar radiation, whereas at the TOA, absorption reduces forcing and scattering increases forcing (Figure 10). Because aerosol absorption is also effective at reducing radiation reflected from the surface, TOA aerosol forcing in the presence of absorbing aerosols is particularly sensitive to surface albedo. This effect is most apparent with black carbon aerosol (the only aerosol component which produces a positive forcing at the TOA) for which  $\beta_T$  ranges from  $5 \text{ W m}^{-2} \tau^{-1}$  over the dark ocean surface to more than  $86 \text{ W m}^{-2} \tau^{-1}$  over the bright Plateau of Tibet. TOA forcing efficiency by the relatively conservative dust model used here is negative everywhere, even over the bright desert surfaces. Dust forcing efficiency over ocean is about  $-40 \text{ W m}^{-2} \tau^{-1}$  and is moderated by bright surfaces (which enhances dust absorption and reduces contrast) and large dust loadings. The sulfate/OC categories, which include a small absorption have a forcing efficiency over ocean of about  $-30 \text{ W m}^{-2} \tau^{-1}$ . This forcing is moderated where relative humidity is low, surface albedo is high, and where concentrations are large. Total TOA aerosol forcing efficiency over ocean is  $\sim -30 \text{ W m}^{-2} \tau^{-1}$  and shows very little variation compared to the surface forcing efficiency.

[33] Regional aerosol forcing at the surface is shown in Figure 11, and at the TOA in Figure 12. Each illustration shows both total forcing and breaks down the forcing into component species. Because of nonlinearities in the radiative transfer, total forcing in Figures 11a and 12a is not equal to the sum of the forcing by the components. (*Collins et al.* [2002] show that the difference between the total forcing and the sum of the components is small for typical aerosol loadings.) As noted previously, the largest forcing is contributed by dust aerosol due to the strong dust storm during the 5–15 April period. The forcing over land is significantly larger than over ocean.

## 5. Evaluation Against *R.H. Brown* Radiometric Observations

[34] *Markowicz et al.* [2003] present detailed observational estimates of radiative forcing efficiency and radiative forcing using pyranometer and sunphotometer measurements on the *R.H. Brown*. The key features of these observations are that the mean optical depth in the Sea of Japan was 0.43, the mean surface forcing was  $-26 \text{ W m}^{-2}$ , and the mean surface forcing efficiency was  $-60 \text{ W m}^{-2} \tau^{-1}$ . These observations compare very well with CFORS/MCRTM predictions averaged over the 7–15 April Sea of Japan leg. Predicted mean optical depth, forcing efficiency and surface forcing are, respectively, 0.33,  $-61 \text{ W m}^{-2} \tau^{-1}$  and  $-20 \text{ W m}^{-2}$  for the external mixing model and 0.34,  $-69 \text{ W m}^{-2} \tau^{-1}$ , and  $-22.5 \text{ W m}^{-2}$  for the internal mixing model. *Markowicz et al.* [2003] find a  $-27.5 \text{ W m}^{-2} \tau^{-1}$  forcing efficiency at the TOA, and a corresponding  $-12.7 \text{ W m}^{-2}$  TOA forcing. The external model estimates  $-32.7 \text{ W m}^{-2} \tau^{-1}$  compared to the more absorptive internal model, which predicts a  $\beta_T$  of  $-28 \text{ W m}^{-2} \tau^{-1}$  efficiency. The external and internal models predict mean TOA forcings of  $-10.8$  and  $-9.5 \text{ W m}^{-2}$ , respectively.

[35] The model-observation comparison is examined more carefully in Table 3, which shows day-to-day variations between observed and modeled optical depth, forcing

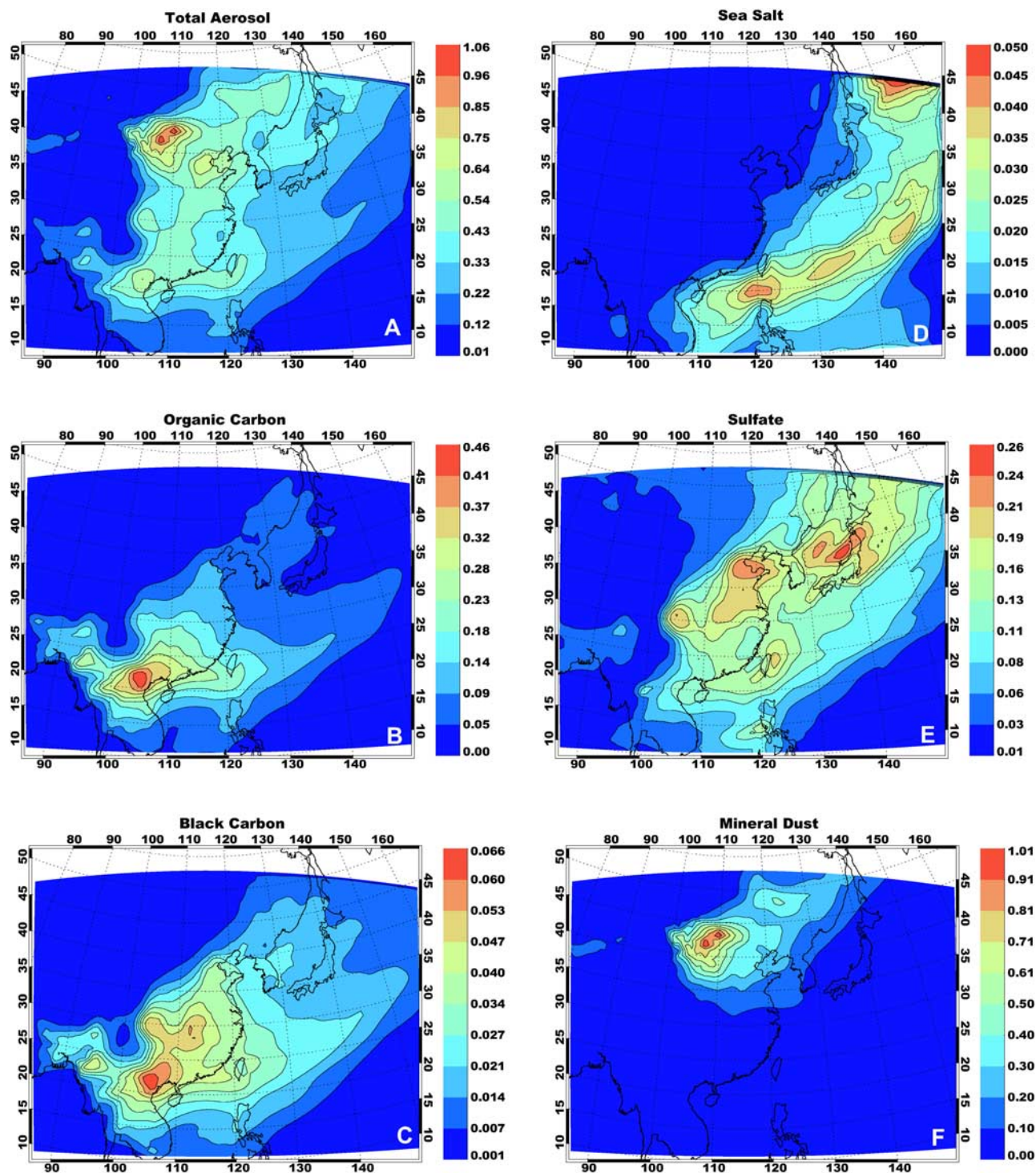


**Figure 8.** Optical depth predicted for (a) all aerosol, (b) organic carbon, (c) black carbon, (d) sea salt, (e) sulfate, and (f) mineral dust. Calculations are for the external model.

efficiency, direct forcing, and single-scatter albedo. (The values of forcing and forcing efficiency are slightly different than those presented by *Markowicz et al.* [2003] because of the use of the *Conant* [2000a] method for clear-sky determination, which finds segments of clear sky on two days in addition to those identified by *Markowicz et al.* [2003] and the MCRTM model for determination of aerosol-free (Rayleigh) surface irradiance. The mean forcing efficiencies

predicted by the two methods are within  $0.5 \text{ W m}^{-2} \tau^{-1}$  of each other.) The model picks up the effects that day-to-day variations in aerosol composition and abundance have on forcing efficiency and optical depth, resulting in an accurate prediction of aerosol forcing and variability in the forcing. One discrepancy between the modeled and observed forcing occurs on 9 April, when observations show a large aerosol plume that is not predicted by the CFORS model. In the

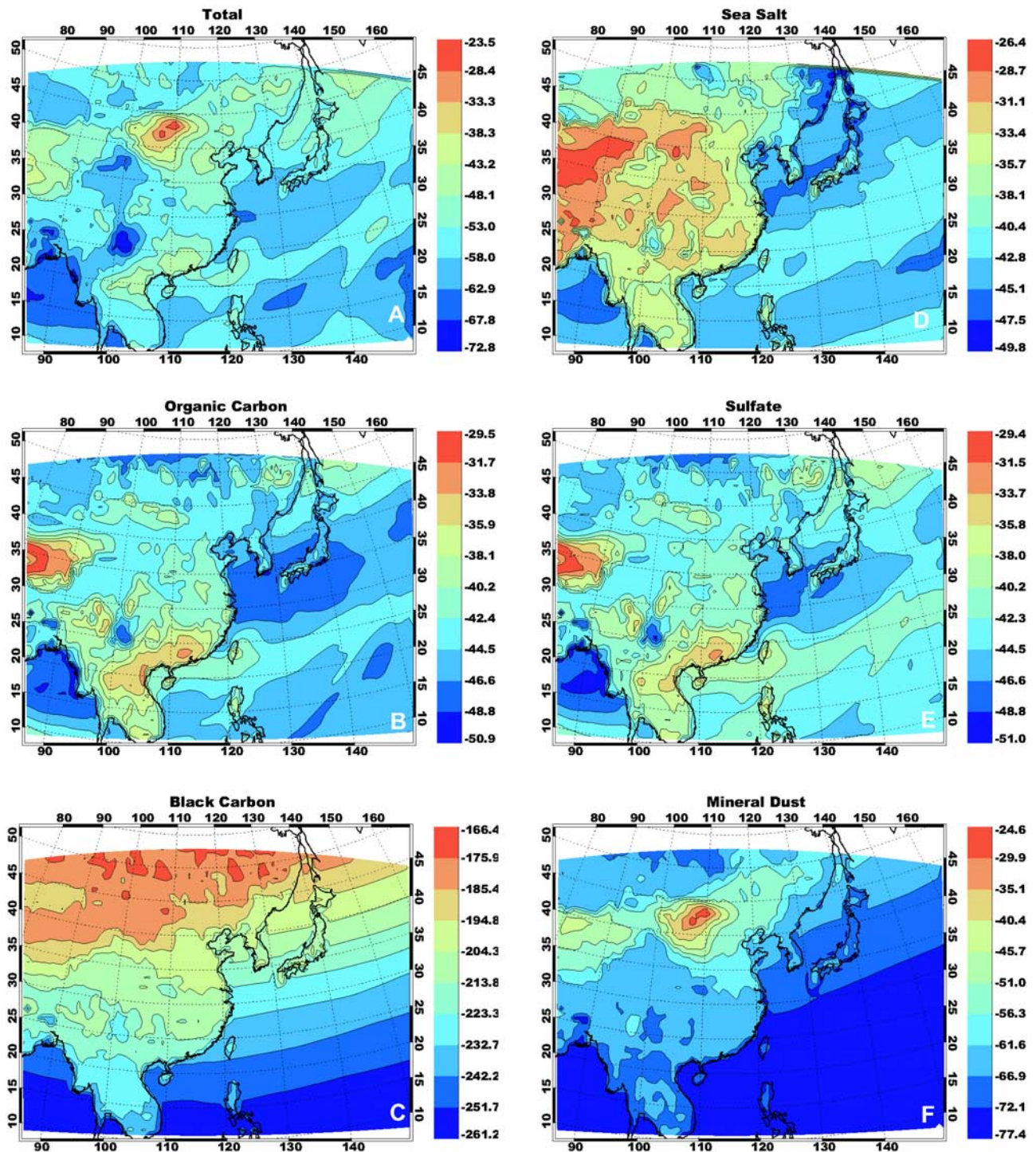


**Figure 9.** Same as Figures 8a–8f, but for surface forcing efficiency. Values are in  $\text{W m}^{-2}$  per unit optical depth at 500 nm.

above, comparisons of forcing efficiencies primarily test how well aerosol optical properties are represented in the model, and comparisons of optical depth primarily test how well aerosol distribution is represented. Much of the difference in optical depth can be attributed to the fact the model did not pick up the pollution/dust plume on 9 April. Regardless, the better agreement in the magnitude and range

of observed and modeled surface and TOA forcing efficiencies is encouraging.

[36] The ideal comparison would be a column closure study between the forcing observed on the *R.H. Brown*, and that predicted by MCRTM using an atmosphere constrained by collocated Twin Otter vertical profiles on one of the three days when the Twin Otter flew within 10 km of the

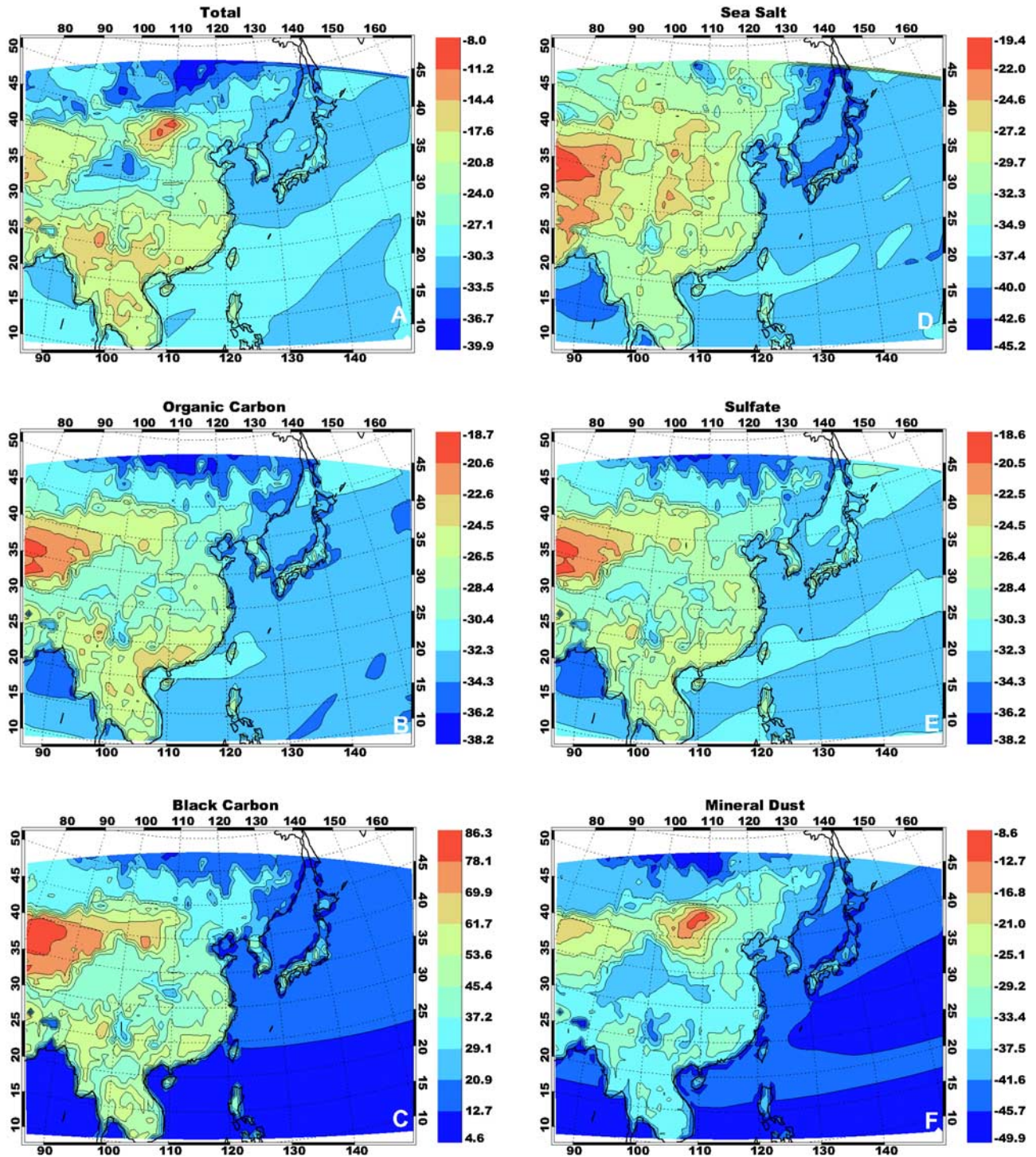


**Figure 10.** Same as Figures 8a–8f, but for TOA forcing efficiency. Values are in  $\text{W m}^{-2}$  per unit optical depth at 500 nm.

ship. Such an attempt is not made here, because only one of the overflight days was sufficiently clear to make forcing measurements, and on that day measurements of supermicrometer aerosol size and aerosol absorption were not available. However, confidence in the aerosol properties used in the aerosol model has been provided by the study of Wang *et al.* [2002], who show that optical depths predicted from the Twin Otter aerosol physico-chemical measurements are in excellent agreement with simultaneously

measured spectral optical depths observed by sunphotometers on board the aircraft.

## 6. Discussion and Conclusions

[37] It is interesting to compare the radiative forcing seen during ACE-Asia to that seen during the Indian Ocean Experiment (INDOEX). The observed surface forcing efficiency was  $-72 \text{ W m}^{-2} \tau^{-1}$  during INDOEX,

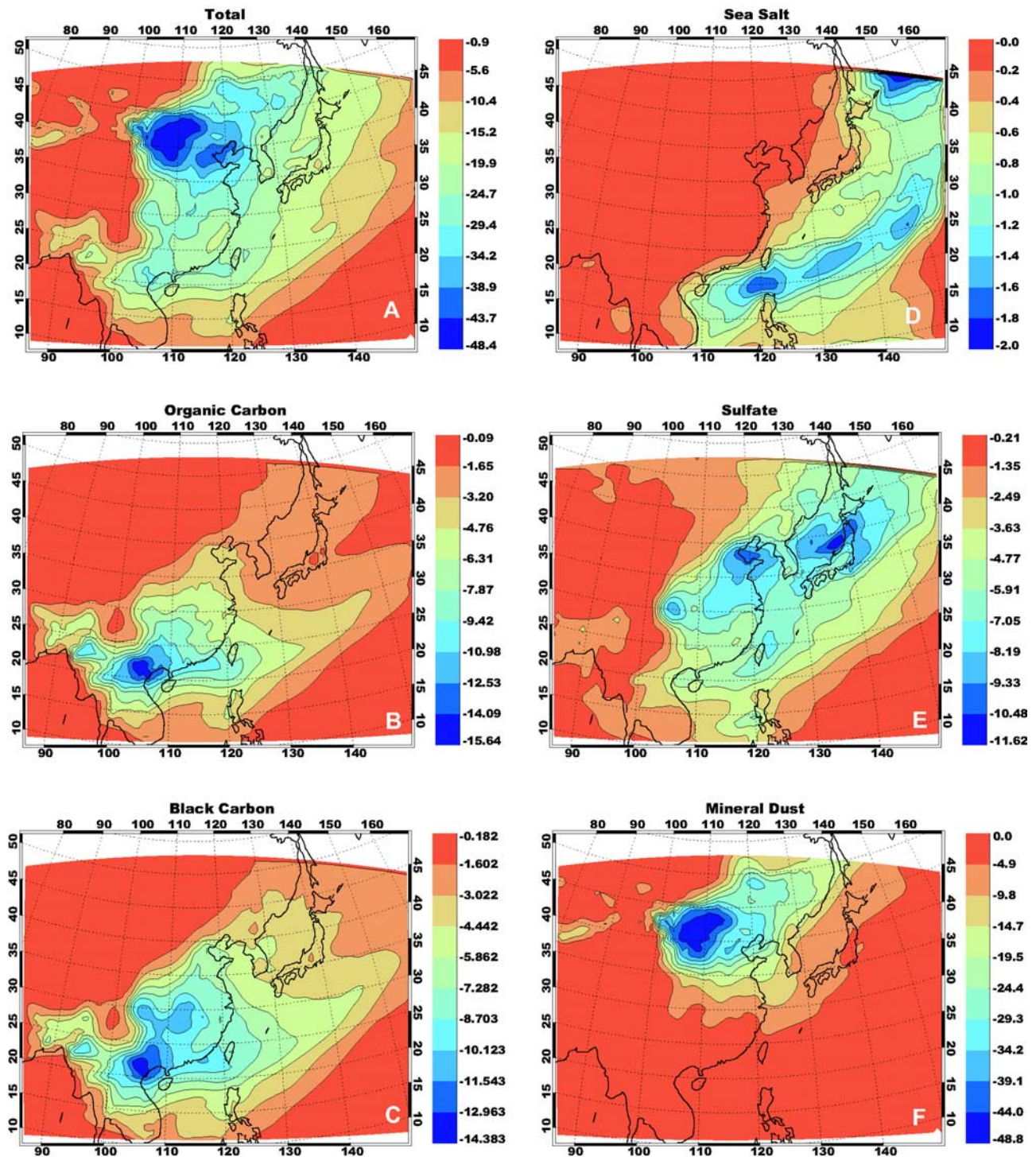


**Figure 11.** Same as Figures 8a–8f, but for surface forcing ( $\text{W m}^{-2}$ ).

compared to a more moderate  $-60 \text{ W m}^{-2} \tau^{-1}$  seen here. Likewise, there was a weaker TOA forcing efficiency during INDOEX ( $-25 \text{ W m}^{-2} \tau^{-1}$ ) compared to ACE-Asia ( $-27.5 \text{ W m}^{-2} \tau^{-1}$ ). Compared to INDOEX, ACE-Asia had a smaller (clear-sky) surface/TOA forcing ratio (2.2 versus 3). To first order, this difference can be attributed to a smaller fraction of black carbon aerosol present in the ACE-Asia pollution mode than seen during INDOEX.

[38] The all-sky (clear + clouds) average surface forcing seen here of  $-17 \text{ W m}^{-2}$  similar to the  $-14 \text{ W m}^{-2}$  surface

forcing observed during INDOEX, although the direct TOA forcing during INDOEX was virtually negligible after the effects of clouds are incorporated [Ramanathan *et al.*, 2001]. The primary differences between the radiative forcings by the East Asian and the South Asian aerosol plumes are that the East Asian plume is characterized by (1) a larger influence of dust (of which an uncertain fraction is anthropogenic); (2) a greater radiative influence of high-level and midlevel clouds that reduce aerosol absorption as opposed to the predominant low clouds that enhanced aerosol

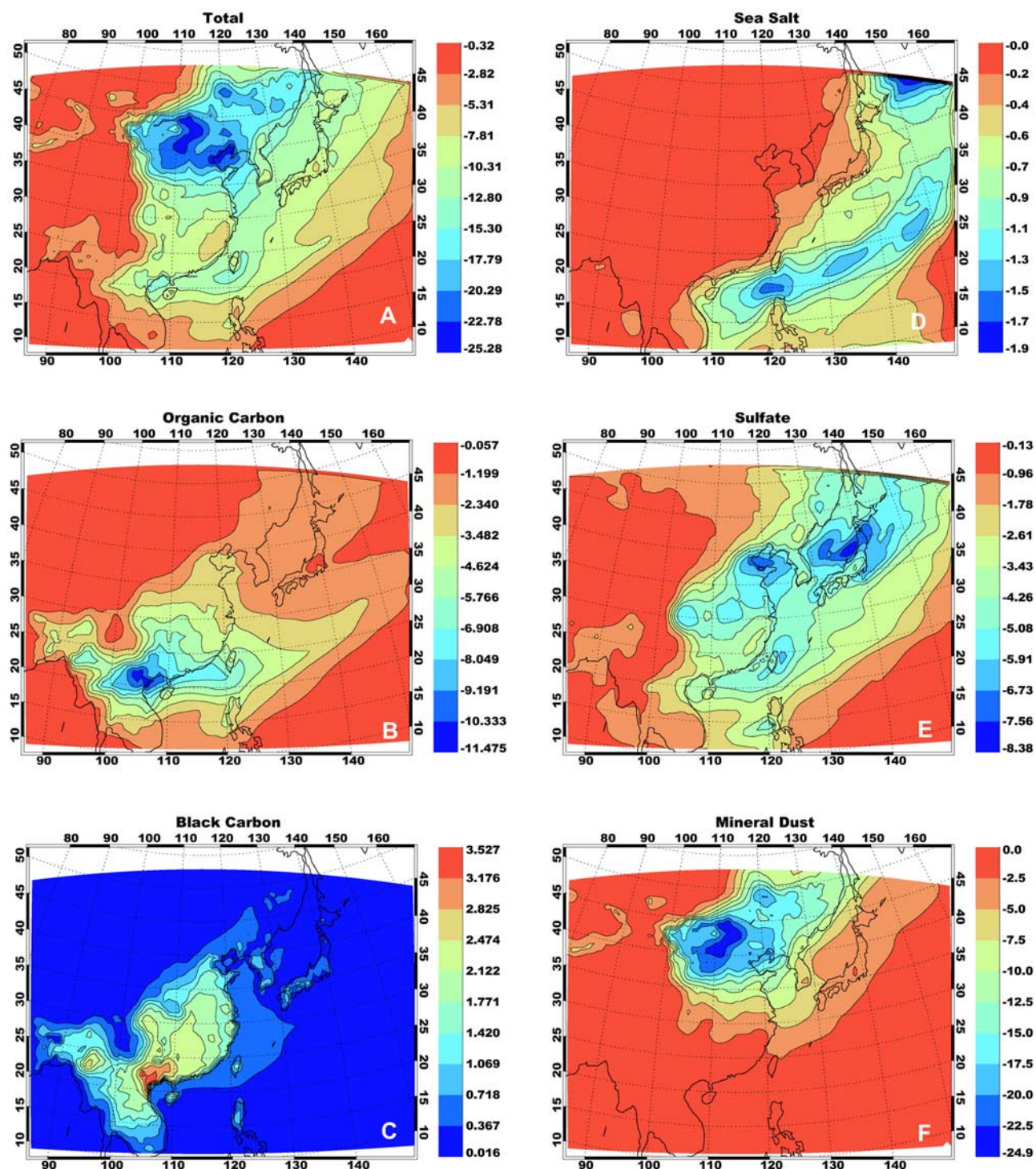


Figure 12. Same as Figures 8a–8f, but for TOA forcing ( $\text{W m}^{-2}$ ).

absorption during INDOEX; and (3) a complex vertical distribution of aerosol due to midlatitude frontal systems.

[39] An interesting result from this study is that dust coated by secondary aerosols, such as sulfate and organic carbon, scatters less radiation than an external mixture of dust and these secondary aerosols. However, when black carbon also coats the dust, the absorptive influence of the BC on the surface and atmospheric heat budgets is not strongly reduced. Thus dust, by acting as an aerosol scavenger, can actually moderate the TOA forcing by

sulfate and organics. In this manner, dust-pollution interactions (i.e., coating) act in the same way as cloud-pollution radiative interactions insofar as TOA forcing is moderated, atmospheric absorption is not moderated, and thus the surface/TOA forcing ratio (an important indicator of aerosol's relative effect on the hydrological cycle [Ramanathan *et al.*, 2001]) is increased.

[40] In summary, regional radiative forcing at the surface and TOA is predicted to be  $-17 \text{ W m}^{-2}$  at the surface, and  $-3 \text{ W m}^{-2}$  at the TOA for the ACE-Asia region from

**Table 3.** Comparison Between Forcing Model and *R.H. Brown* Observations for Properties Relevant to Aerosol Forcing

Day	<i>R.H. Brown</i> (Data for Clear Skies Only)				CFORS + MCRTM Model Estimate External/Internal			
	$\tau$	$\beta_S$	$F_S$	$\omega_0$ (Amb.)	$\tau$	$\beta_S$	$F_S$	$\omega_0$ (Amb.)
6 April	0.34	-45 ± 6	-19	0.94	.20/.20	-65/-75	-13/-15	0.94
7 April	0.44	-60 ± 5	-29	0.95	.25/.25	-63/-75	-16/-19	0.96
8 April	0.33	-50 ± 7	-20	0.96	.28/.28	-58/-65	-16/-18	0.95
9 April	0.82	-62 ± 3	-54	0.96	.28/.29	-65/-76	-18/-22	0.94
10 April	0.68	-51 ± 3	-38	0.98	.43/.43	-52/-56	-22/-24	0.98
12 April	0.52	-80 ± 4	-45	0.94	.64/.65	-61/-65	-39/-42	0.93
13 April	0.24	-65 ± 9	-19	0.92	.31/.31	-66/-72	-20/-22	0.93
15 April	0.18	-57 ± 11	-14	0.91	.13/.13	-67/-72	-9/-9	0.94

20°N–50°N, 100°E–150°E during the 5–15 April 2001 dust storm period. About half of this radiative forcing is due to mineral dust. The subset of these predictions that overlap with the cruise of the *R.H. Brown* show generally good agreement on the value of both forcing efficiency and total forcing by the aerosol.

[41] **Acknowledgments.** This work was supported by Office of Naval Research grant N00014-96-1-0119 and National Science Foundation grant ATM-0001934. P.J.F. was supported by ONR program element PE0602435N and by the NSF climate and chemistry programs. S.J. Masonis provided helpful feedback on an earlier version of the manuscript.

## References

- Briegleb, B., P. Minnis, V. Ramanathan, and E. Harrison, Comparison of regional clear-sky albedos inferred from satellite observations and model computations, *J. Clim. Appl. Meteorol.*, **25**, 214–226, 1986.
- Buseck, P. R., and M. Posfai, Airborne minerals and related aerosol particles: Effects on climate and the environment, *Proc. Natl. Acad. Sci. U. S. A.*, **96**, 3372–3379, 1999.
- Chylek, P., G. B. Lesins, G. Videen, J. G. D. Wong, R. G. Pinnick, D. Ngo, and J. D. Klett, Black carbon and absorption of solar radiation by clouds, *J. Geophys. Res.*, **101**, 23,365–23,371, 1996.
- Claquin, T., M. Schultz, S. Balkanski, and O. Boucher, Uncertainties in assessing radiative forcing by mineral dust, *Tellus, Ser. B*, **50**, 491–505, 1998.
- Collins, W. D., P. J. Rasch, B. E. Eaton, D. W. Fillmore, and J. T. Kiehl, Simulation of aerosol distributions and radiative forcing for INDOEX: Regional climate impacts, *J. Geophys. Res.*, **107**(D19), 8028, doi:10.1029/2000JD000032, 2002.
- Conant, W. C., An observational approach for determining aerosol surface radiative forcing: Results from the first field phase of INDOEX, *J. Geophys. Res.*, **105**, 15,347–15,360, 2000a.
- Conant, W. C., Interactions between aerosol, water vapor, and solar radiation, Ph.D. thesis, Univ. of Calif., San Diego, La Jolla, 2000b.
- Fuller, K. A., W. C. Malm, and S. M. Kreidenweis, Effects of mixing on extinction by carbonaceous particles, *J. Geophys. Res.*, **104**, 15,941–15,954, 1999.
- Gao, Y., and J. R. Anderson, Characteristics of Chinese aerosols determined by individual-particle analysis, *J. Geophys. Res.*, **106**, 18,037–18,045, 2001.
- Gong, S. L., L. A. Barrie, and J. P. Blanchet, Modeling sea-salt aerosols in the atmosphere: I. Model development, *J. Geophys. Res.*, **102**, 3805–3818, 1997.
- Hess, M., P. Koepke, and I. Schult, Optical properties of aerosols and clouds: The software package OPAC, *Bull. Am. Meteorol. Soc.*, **79**, 831–844, 1998.
- Houghton, J. T., Y. Ding, D. J. Griggs, M. Noguer, P. J. van der Linden, and D. Xiaosu (Eds.), *Climate Change 2001: The Scientific Basis*, 944 pp., Cambridge Univ. Press, New York, 2001.
- Jayaraman, A., D. Lubin, S. Ramachandran, E. Woodbridge, W. D. Collins, and K. S. Zalpuri, Direct observations of aerosol radiative forcing over the tropical Indian Ocean during the January–February pre-INDOEX cruise, *J. Geophys. Res.*, **103**, 13,827–13,836, 1998.
- Kaufman, Y. J., D. Tanre, O. Dubovik, A. Karnieli, and L. A. Remer, Absorption of sunlight by dust as inferred from satellite and ground-based remote sensing, *Geophys. Res. Lett.*, **28**, 1479–1482, 2001.
- Lee, S.-H., D. M. Murphy, D. S. Thomson, and A. M. Middlebrook, Chemical components of single particles measured with Particle Analysis by Laser Mass Spectrometry (PALMS) during the Atlanta SuperSite Project: Focus on organic/sulfate, lead, soot, and mineral particles, *J. Geophys. Res.*, **107**(D1), 4003, doi:10.1029/2000JD000011, 2002.
- Mader, B. T., R. C. Flagan, and J. H. Seinfeld, Aircraft measurements of atmospheric carbonaceous aerosols during ACE-Asia, *J. Geophys. Res.*, **107**(D23), 4704, doi:10.1029/2002JD002221, 2002.
- Markowicz, K. M., P. J. Flatau, P. K. Quinn, C. M. Carrico, M. K. Flatau, A. M. Vogelmann, D. Bates, M. Liu, and M. J. Rood, Influence of relative humidity on aerosol radiative forcing: An ACE-Asia experiment perspective, *J. Geophys. Res.*, **108**(D23), 8662, doi:10.1029/2002JD003066, in press, 2003.
- Mishchenko, M. I., and L. D. Travis, Light scattering by polydispersions of randomly oriented spheroids with sizes comparable to wavelengths of observation, *Appl. Opt.*, **33**, 7206–7225, 1994.
- Nenes, A., S. N. Pandis, and C. Pilinis, ISORROPIA: A new thermodynamic equilibrium model for multiphase multicomponent inorganic aerosols, *Aquat. Geochem.*, **4**, 123–152, 1998.
- Pielke, R. A., et al., A comprehensive meteorological modeling system: RAMS, *Meteorol. Atmos. Phys.*, **49**, 69–91, 1992.
- Podgorny, I. A., W. C. Conant, V. Ramanathan, and S. K. Satheesh, Aerosol modulation of atmospheric and surface solar heating over the tropical Indian Ocean, *Tellus, Ser. B*, **52**, 947–958, 2000.
- Ramanathan, V., R. D. Cess, E. F. Harrison, P. Minnis, B. R. Barkstrom, E. Ahmad, and D. Hartmann, Cloud-radiative forcing and climate: Results from the Earth Radiation Budget Experiment, *Science*, **243**, 57–63, 1989.
- Ramanathan, V., P. J. Crutzen, J. T. Kiehl, and D. Rosenfeld, Aerosols, climate, and the hydrological cycle, *Science*, **294**, 2119–2124, 2001.
- Rossov, W. B., and R. A. Schiffer, ISCCP cloud data products, *Bull. Am. Meteorol. Soc.*, **72**, 2–20, 1991.
- Satheesh, S. K., and V. Ramanathan, Large differences in tropical aerosol forcing at the top of the atmosphere and Earth's surface, *Nature*, **405**, 60–63, 2000.
- Sellers, P. J., D. A. Randall, C. J. Collatz, J. A. Berry, C. B. Field, D. A. Dazlich, C. Zhang, and C. D. Collelo, A revised land surface parameterization (SiB2) for atmospheric GCMs. Part 1: Model formulation, *J. Clim.*, **9**, 676–705, 1996.
- Shettle, E. P., and R. W. Fenn, Models for the aerosols of the lower atmosphere and the effects of humidity variation on their optical properties, *Rep. AFGL-TR-79-0214*, Air Force Geophys. Lab., Hanscom Air Force Base, Mass., 1979.
- Sokolik, I. N., and O. B. Toon, Incorporation of mineralogical composition into models of the radiative properties of mineral aerosol from UV to IR wavelengths, *J. Geophys. Res.*, **104**, 9423–9444, 1999.
- Streets, D. G., N. Y. Tsai, H. Akimoto, and K. Oka, Sulfur dioxide emissions in Asia in the period 1985–1997, *Atmos. Environ.*, **34**, 4413–4424, 2000.
- Streets, D. G., S. Gupta, S. T. Waldhoff, M. Q. Wang, T. C. Bond, and Y. Y. Bo, Black carbon emissions in China, *Atmos. Environ.*, **35**, 4281–4296, 2001.
- Toon, O. B., and T. P. Ackerman, Algorithms for the calculation of scattering by stratified spheres, *Appl. Opt.*, **20**, 3657–3660, 1981.
- Uno, I., et al., Regional chemical weather forecasting system CFORS: Model descriptions and analysis of surface observations at Japanese island stations during the ACE-Asia experiment, *J. Geophys. Res.*, **108**(D23), 8668, doi:10.1029/2002JD002845, 2003.
- Wang, J., et al., Clear-column radiative closure during ACE-Asia: Comparison of multiwavelength extinction derived from particles size and composition with results from Sun photometry, *J. Geophys. Res.*, **107**(D23), 4688, doi:10.1029/2002JD002465, 2002.
- G. R. Carmichael and Y. Tang, Center of Global and Regional Environmental Research, University of Iowa, 204 Iowa Advanced Technology Laboratories, Iowa City, IA 52242-1000, USA. (gcarmich@icaen.uiowa.edu; ytang@cgrer.uiowa.edu)
- W. C. Conant, J. H. Seinfeld, and J. Wang, Department of Environmental Sciences and Engineering, California Institute of Technology, Mail Code 210-41, 1200 E. California Boulevard, Pasadena, CA 91125, USA. (wconant@caltech.edu; seinfeld@caltech.edu; jian@bnl.gov)
- P. J. Flatau, Naval Research Laboratory, 7 Grace Hopper Avenue STOP 2, Monterey, CA 93943-5502, USA. (pflatau@ucsd.edu)
- K. M. Markowicz, University of Warsaw, Pasteura 7, 02093 Warsaw, Poland. (kmark@igf.fuw.edu.pl)
- P. K. Quinn, Pacific Marine Environmental Laboratory, NOAA, 7600 Sand Point Way, NE, Seattle, WA 98115, USA. (quinn@pmel.noaa.gov)
- I. Uno, Research Institute for Applied Mechanics, Kyushu University, Kasuga, 816-8580, Fukuoka, Japan. (iuno@riam.kyushu-u.ac.jp)